

Softening vs. Hardening Nonlinear Energy Sinks: Forced Vibration Control and Isolated Resonance Curves

Kevin Dekemele, Giuseppe Habib

Abstract

The nonlinear energy sink (NES) is a practical passive device for vibration control that has gained significant attention due to its ability to mitigate resonant vibrations across a wide frequency range. Conventional NES designs typically employ a hardening restoring force, which enables broad operational frequency coverage but faces limitations in the operational amplitude range, also due to the emergence of isolated resonance curves (IRCs). This study investigates a softening NES, where the restoring force characteristic is modeled as a saturating function. Analytical results demonstrate that the softening NES retains the beneficial amplitude saturation effect and strongly modulated response (SMR) observed in hardening NESs, while significantly expanding the range over which SMR occurs. Furthermore, the IRCs in the softening NES appear on the right of the resonance peak, unlike the leftward location in hardening NESs, making it advantageous for applications where excitation frequency ramps up. Notably, IRCs in the softening NES are less detrimental as they result in smaller amplitude jumps. We also identify parameter values that suppress the formation of IRCs without compromising the performance of the NES, providing a practical advantage over conventional designs. Despite these promising findings, the practical realization of the softening NES remains an open challenge, which will be the focus of future research. Overall, the softening NES exhibits superior performance compared to the hardening NES, presenting an effective alternative for vibration suppression in various engineering applications.

1 Introduction

Vibration mitigation is a critical challenge in various engineering systems, where excessive oscillations can lead to structural fatigue, operational inefficiencies, or even catastrophic failure. Among passive vibration control devices, tuned mass dampers (TMDs) have long been one of the most effective and widely used tools [1, 2, 3]. TMDs operate by adding a secondary mass-spring-damper system tuned to the natural frequency of the host structure, effectively counteracting resonant vibrations through modal interaction. However, their applicability is

limited by their narrow operational frequency range. This makes TMDs unsuitable for systems with multiple dominant frequencies or those whose natural frequencies vary due to changing operational conditions, such as temperature fluctuations or structural degradation.

The nonlinear energy sink (NES) offers a valid alternative to TMDs, overcoming many of these limitations. Unlike TMDs, the NES employs a nonlinear restoring force, which allows it to resonate across multiple frequencies. This property gives the NES a much broader operational frequency bandwidth. Over the past two decades, the NES has been the subject of extensive research, resulting in thousands of studies [4] and numerous design variations [5, 6]. Despite this diversity, the most common NES configuration relies on a purely cubic hardening restoring force, and its dynamics have been studied under various loading conditions, including transient [7, 8], harmonic [9, 10], self-excited [11, 12], parametric [13], and stochastic excitations [14].

Under transient loading, the NES engages in targeted energy transfer (TET), where vibrational energy from the primary system is transferred to the NES and dissipated [15]. In systems with multiple natural frequencies, this energy transfer occurs sequentially through the so-called resonance capture cascade (RCC), where the NES tunes itself to each frequency in turn, enabling effective mitigation of multi-modal vibrations [16, 17, 18]. For self-excited oscillations, the NES has limited impact on the stability of the system [19] but can significantly reduce the amplitude of oscillations, thereby improving operational performance [20].

Under harmonic excitation – which is the focus of this study – the NES exhibits distinct regimes of operation depending on the amplitude of the excitation. At low excitation levels, the NES remains practically inactive, which is not a concern since small-amplitude vibrations are generally not problematic. Beyond a critical energy threshold, the NES becomes active, causing the vibration amplitude of the host system to saturate, remaining nearly constant, even as the forcing amplitude increases. This saturation effect is a hallmark of the NES's effectiveness in vibration control [21].

For excitation amplitudes near this threshold, the NES transitions into a strongly modulated response (SMR) regime, characterized by quasiperiodic motions and continuous energy exchange between the host system and the NES [22]. During SMR, the oscillation amplitude of the host system remains comparable to the saturation level, making it a favorable regime for vibration mitigation. However, as the excitation amplitude increases further, isolated resonance curves (IRCs) are triggered. These IRCs typically result in significantly larger oscillation amplitudes in the host system, marking the upper limit of the NES's effective operational range. Beyond this point, any further increase in forcing amplitude leads to an almost proportional increase in the vibration amplitude of the host system, making the NES ineffective.

IRCs are branches of periodic solutions that are disconnected from the main resonance branch in the frequency response (FR) of a vibrating system. One of the first studies about them dates back to 1955 [23] when they were discovered in softening Duffing oscillators. Although initially they were considered a relatively

exhotic phenomenon [24], later studies illustrated that they are present in several dynamical systems, including systems with hysteresis [25, 26, 27], systems subject to nonlinear damping [28, 29], systems with discontinuities [30, 31, 32], in the case of sub- or super-harmonic resonances [33, 34, 35], and in the presence of internal resonances [36, 37].

IRCs' topology makes them particularly elusive; in fact, they are overlooked by standard continuation techniques, both experimentally and numerically. Conversely, they can be identified through approximation techniques, which transform the system's dynamics governing differential equations into a system of algebraic equations. This can be achieved through, e.g., multiple-scale techniques [38], averaging [29], or harmonic balance [39]. Alternatively, techniques investigating a system's global dynamics can also help to identify IRCs [33, 40].

IRCs are very common in nonlinear dynamic vibration absorbers [41, 42], and in most cases detrimental, as they are usually related to a small activation of the vibration absorber, leading to large oscillations of the primary system [39].

Referring to NESs, IRCs are ubiquitous. Typically, an IRC coexists with a SMR [43]. Differently from SMR, IRCs are usually associated with an almost negligible NES effectiveness [12]. This scenario motivated extensive research to develop methods for the elimination of IRCs. An obvious strategy consists of selecting parameter values for which there are no IRCs, as done, for example, in [42] exploiting singularity theory. However, this typically requires compromising the NES performance. In [43], it was illustrated that an NES with a nonlinear damping characteristic eliminates the detrimental IRC without reducing its performance. A similar approach was implemented in [44], where conditions leading to detrimental IRCs were identified, highlighting that, in some cases, they are not.

Recently, a novel NES presenting a softening and saturating restoring force function was developed [45]. This NES, besides exhibiting an inverted RCC (from low to high frequency) when subject to shock vibrations [45], can mitigate vibrations also at very low energetic levels, as numerically demonstrated in [46, 47], and applied to a cantilever beam in [48], where a fractional power characteristic describes the NES's restoring force function.

Although dynamic vibration absorbers with a purely softening restoring force characteristic have never been realized in practice, several mechanisms with this property exist, such as constant force [49, 50] or constant torque [51, 52] devices. These systems, exhibiting a softening and/or saturating force-displacement characteristic, could be modified to serve as softening NESs.

This study investigates the performance of a softening NES to control harmonically excited oscillations of a host system. The study is carried out analytically by exploiting the complexification-averaging method, which leads to an analytical expression of the slow invariant manifold (SIM), later used for characterizing the system dynamics. In particular, periodic motions, SMRs, and IRCs are identified, and their relevance to the NES performance is evaluated. Later, singularity theory is used to identify parameter values where IRCs are absent

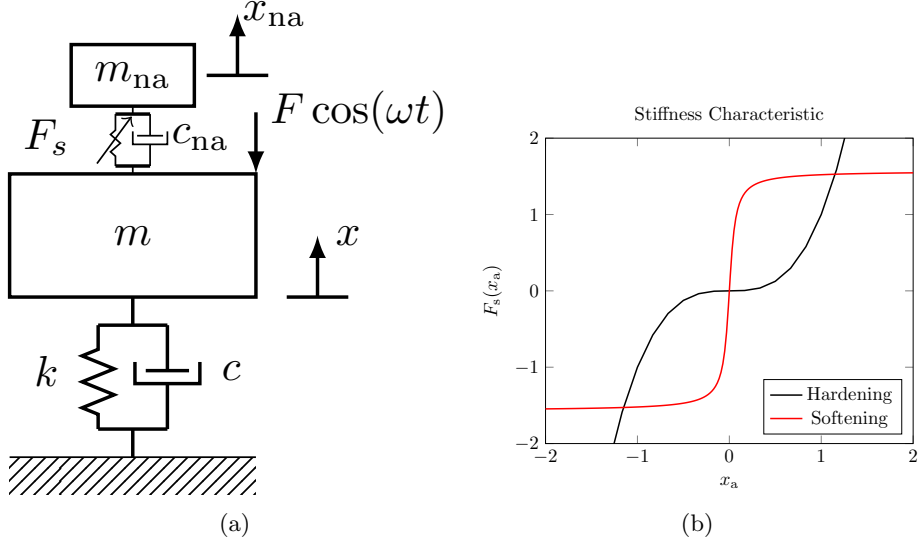


Figure 1: Scheme of flexible mechanical system (a) and stiffness characteristic (b). The conventional stiffness is x_a^3 while the saturating is $\arctan(20x_a)$.

[44, 53]. All results for the softening NES are compared with a classical cubic hardening NES. The rest of the paper is structured as follows. In Section 2, the equations of motion are presented and non-dimensionalized. Section 3 derives the FR of the system and SMR obtained from a complexification-averaging procedure. Section 4 investigates the IRCs. In Section 5, the performance of hardening and softening NES are compared, after which the conclusions are presented.

2 Equations of motion and nondimensionalization

The system under consideration is a nonlinear energy sink coupled to a harmonically forced linear single degree-of-freedom (DOF) host system, as illustrated in Figure 1a. The equations of motion (EOM) are:

$$\begin{aligned} m\ddot{x} + c\dot{x} + kx + c_{na}(\dot{x} - \dot{x}_{na}) + F_s(x - x_{na}) &= F \cos(\omega t) \\ m_{na}\ddot{x}_{na} + c_{na}(\dot{x}_{na} - \dot{x}) + F_s(x_{na} - x) &= 0 \end{aligned} \quad (1)$$

where m , c , k are the host system's mass, viscous damping and stiffness coefficients, and m_{na} , c_{na} , $F_s(\cdot)$ are the NES's mass, viscous damping and nonlinear stiffness, respectively. x and x_{na} mark the displacement of the host system and the NES, respectively. A harmonic load is applied to the host system with magnitude F and frequency ω . The EOM are also valid for larger dimensional

systems, assuming no modal interactions are present, where the coefficients refer to modal quantities. Two stiffness characteristics ($F_s(\cdot)$) are considered, the conventional hardening cubic stiffness and a saturating stiffness, leading to softening behavior; these are shown in Figure 1b. The functions describing these characteristics are:

$$F_s(z) = \begin{cases} k_{na}z^3 \\ k_{sat} \arctan(k_s z) \end{cases} \quad (2)$$

where k_{na} is the coefficient of the hardening stiffness, $2k_{sat}/\pi$ is the force level where the arctan saturates and k_s is the internal coefficient of the arctan. Around the origin, the arctan is approximately linear with slope $k_{sat}k_s$.

To reduce the number of parameters to be studied, the EOM in (1) are non-dimensionalized. Considering the dimensionless time $\tau = \omega_n t$ and introducing the relative absorber displacement ($z = x_{na} - x$), the EOM become:

$$\begin{aligned} x'' + \varepsilon \xi x' + x + \varepsilon (z'' + x'') &= \varepsilon P \cos(\Omega \tau) \\ \varepsilon (z'' + x'') + \varepsilon \xi_{na} z' + \varepsilon f_s(z) &= 0 \end{aligned} \quad (3)$$

where

$$\begin{aligned} \varepsilon &= \frac{m_{na}}{m}, \quad \xi = \frac{c}{m_{na}\omega_n}, \quad \xi_{na} = \frac{c_{na}}{m_{na}\omega_n}, \quad f_s(z) = \frac{F_s(z)}{m_{na}\omega_n^2}, \\ P &= \frac{F}{\omega_n^2 m_{na}}, \quad \Omega = \frac{\omega}{\omega_n}, \quad ' \circ = \frac{d}{d\tau}. \end{aligned} \quad (4)$$

The nonlinear restoring forces are:

$$F_s = k_3 z^3 \Rightarrow f_s = \gamma z^3, \quad F_s = k_{sat} \arctan(k_s z) \Rightarrow f_s = \kappa_{sat} \arctan(k_s z) \quad (5)$$

where

$$\gamma = \frac{k_3}{m_{na}\omega_n^2}, \quad \kappa_{sat} = \frac{k_{sat}}{m_{na}\omega_n^2}. \quad (6)$$

The displacements are non-dimensionalized to \bar{x} and \bar{z} . The way of nondimensionalization depends on the type of stiffness:

$$\begin{aligned} f_s(z) = \gamma z^3 \Rightarrow \bar{z} &= \sqrt{\gamma} z, \quad \bar{x} = \sqrt{\gamma} x \Rightarrow f_s(\bar{z}) = \bar{z}^3 \\ f_s(z) = \kappa_{sat} \arctan(k_s z) \Rightarrow \bar{z} &= k_s z, \quad \bar{x} = k_s x \Rightarrow f_s(\bar{z}) = \kappa \arctan(\bar{z}) \end{aligned} \quad (7)$$

where $\kappa = \kappa_{sat} k_s = \omega_a^2 / \omega_n^2$

κ is the squared ratio between the linearized natural frequency of the absorber, $\omega_a^2 = k_{sat} k_s / m_{na}$, and the natural frequency of the host system. The dimensionless equations of motion, both in time and displacement, are:

$$\begin{aligned} \bar{x}'' + \varepsilon \xi \bar{x}' + \bar{x} + \varepsilon (\bar{z}'' + \bar{x}'') &= \varepsilon \bar{P} \cos(\Omega \tau) \\ \varepsilon (\bar{z}'' + \bar{x}'') + \varepsilon \xi_{na} \bar{z}' + \varepsilon f_s(\bar{z}) &= 0. \end{aligned} \quad (8)$$

The expression of the dimensionless forcing amplitude \bar{P} depends on the considered characteristic:

$$\begin{aligned} f_s(\bar{z}) = \bar{z}^3 &\Rightarrow \bar{P} = \sqrt{\gamma}P \\ f_s(z) = \kappa_{\text{sat}} \arctan(k_s z) &\Rightarrow \bar{P} = k_s P. \end{aligned} \quad (9)$$

In the next section, the frequency responses for both NESs will be derived.

3 Averaging and frequency response

3.1 Complexification-averaging analysis

The complexification-averaging (CxA) method will be used to obtain the frequency response, [54, 55, 56]. In this procedure, a single vibration frequency (the forcing frequency) is assumed in the displacements \bar{z} and \bar{x} . Then, the vibrations are split into a fast and a slow part. The slow part marks the amplitude modulation of the vibration, while the fast part indicates the vibrations themselves. Finally, the slow part is averaged over the period of the assumed vibration frequency. The following complex Manevitch variables [54] facilitate these steps:

$$2A(\tau)e^{i\tau} = \bar{x} - i\frac{\bar{x}'}{\Omega} \quad 2B(\tau)e^{i\tau} = \bar{z} - i\frac{\bar{z}'}{\Omega} \quad (10)$$

where $i = \sqrt{-1}$ is the imaginary unit and $A(\tau)$ and $B(\tau)$ are complex variables that contain the amplitude and phase modulation. The original variables are then substituted by the complex variables by:

$$\begin{aligned} \bar{x} &= A(\tau)e^{i\Omega\tau} + A^*(\tau)e^{-i\Omega\tau} & \bar{z} &= B(\tau)e^{i\Omega\tau} + B^*(\tau)e^{-i\Omega\tau} \\ \bar{x}' &= i\Omega(A(\tau)e^{i\Omega\tau} - A^*(\tau)e^{-i\Omega\tau}) & \bar{z}' &= i\Omega(B(\tau)e^{i\Omega\tau} - B^*(\tau)e^{-i\Omega\tau}) \\ \bar{x}'' + \Omega^2\bar{x} &= i2\Omega A'e^{i\Omega\tau} & \bar{z}'' + \Omega^2\bar{z} &= i2\Omega B'e^{i\Omega\tau} \end{aligned} \quad (11)$$

Substituting (11) into (8) and averaging over the frequency Ω yields:

$$\begin{aligned} i2\Omega A' + i\varepsilon\xi\Omega A + (1 - \Omega^2)A + \varepsilon(i2\Omega B' - \Omega^2B + i2\Omega A' - \Omega^2A) &= \frac{\varepsilon\bar{P}}{2} \\ i2\Omega B' + 2i\Omega A' - \Omega^2B - \Omega^2A + \xi_{\text{na}}i\Omega B + BG(|B|) &= 0 \end{aligned} \quad (12)$$

In steady state ($A' = B' = 0$), (12) is reduced to:

$$\begin{aligned} i\xi\Omega A + \sigma A - \Omega^2B - \Omega^2A &= \frac{\bar{P}}{2} \\ -\Omega^2B - \Omega^2A + \xi_{\text{na}}i\Omega B + BG(B, B^*) &= 0 \end{aligned} \quad (13)$$

with $\varepsilon\sigma = 1 - \Omega^2$. Next, the equations can be manipulated to obtain two equations in a and b with $A = a e^{i\alpha}/2$ and $B = b e^{i\beta}/2$. The first one is a SIM between a and b :

$$\Omega^4 a^2 = b^2 \left((\Omega^2 \xi_{\text{na}})^2 + (\Omega^2 - G(b))^2 \right), \quad (14)$$

while the second equation, relating b with \bar{P} , is

$$\begin{aligned} & \left([(\Omega^2 - \sigma)(G(b) - \Omega^2) + \Omega^2 \xi_{\text{na}} \xi + \Omega^4]^2 + \Omega^2 [\xi(G(b) - \Omega^2) + (\sigma - \Omega^2)(\xi_{\text{na}})]^2 \right) b^2 \\ &= (\Omega^2 \bar{P})^2. \end{aligned} \quad (15)$$

The term $G(b)$ depends on the type of stiffness characteristic, according to the following equation [57]:

$$be^{j\beta} G(b) = \frac{\Omega}{2\pi} \int_0^{\frac{2\pi}{\Omega}} f_s \left(\frac{be^{j(\Omega\tau+\beta)} + be^{-j(\Omega\tau+\beta)}}{2} \right) e^{-j\Omega\tau} d\tau. \quad (16)$$

This term is computed for the hardening and the softening stiffness in Appendix A. The stability of the steady state solutions of (13) and of the SIM are computed in Appendices B and C.

3.2 Hardening stiffness $f_s(\bar{z}) = \bar{z}^3$

If $f_s(\bar{z}) = \bar{z}^3$ then $G(b) = \frac{3}{4}b^2$. The SIM equations is then

$$\Omega^4 a^2 = b^2 \left((\Omega \xi_{\text{na}})^2 + \left(\Omega^2 - \frac{3}{4}b^2 \right)^2 \right) \quad (17)$$

and the relation between b and \bar{P} is given by

$$\begin{aligned} & b^6 \left(\left((\Omega^2 - \sigma) \frac{3}{4} \right)^2 + \Omega^2 \left(\xi \frac{3}{4} \right)^2 \right) \\ &+ b^4 \left(2 \left((\Omega^2 - \sigma) \frac{3}{4} \right) (-\Omega^2 (\Omega^2 - \sigma) + \Omega^2 \xi_{\text{na}} \xi + \Omega^4) + 2\Omega^2 \left(\xi \frac{3}{4} \right) (\xi(-\Omega^2) + (\sigma - \Omega^2) \xi_{\text{na}}) \right) \\ &+ b^2 \left(((\Omega^2 - \sigma) (-\Omega^2) + \Omega^2 \xi_{\text{na}} \xi + \Omega^4)^2 + \Omega^2 (\xi(-\Omega^2) + (\sigma - \Omega^2) \xi_{\text{na}})^2 \right) \\ &- \Omega^4 \bar{P}^2 = 0. \end{aligned} \quad (18)$$

By identifying the maximum and minimum values of the SIM, the saturation amplitude of the host system under SMR can be estimated. These points are found by derivation of (17) w.r.t. b^2 and finding the roots of the obtained equations. This leads to the following equations for the maximum and minimum values:

$$\begin{aligned} b_{\pm}^2 &= \frac{8}{9}\Omega^2 \pm \frac{4}{9}\sqrt{\Omega^4 - 3\Omega^2 \xi_{\text{na}}^2} \\ \Omega^4 a_{\mp}^2 &= b_{\pm}^2 \left((\Omega \xi_{\text{na}})^2 + \left(\Omega^2 - \frac{3}{4}b_{\pm}^2 \right)^2 \right). \end{aligned} \quad (19)$$

The SIM and these points for the hardening stiffness are visualized in red in Figure 2. During SMR, the amplitude of the host system modulates between

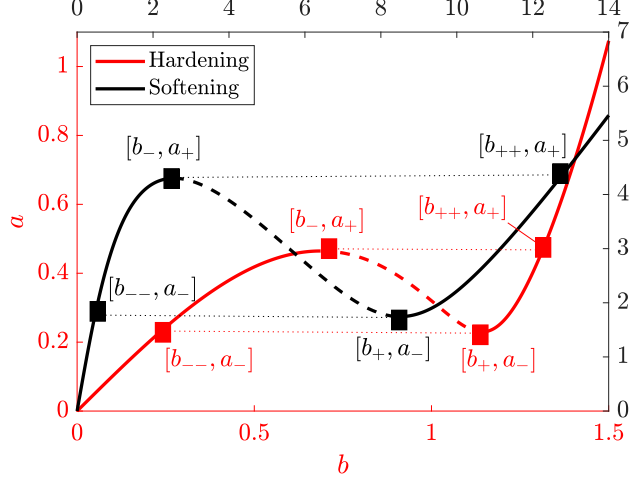


Figure 2: Slow invariant manifolds for hardening ($\xi_{na} = 0.2$, $\Omega = 1$) and saturating NESs ($\xi_{na} = 0.2$, $\Omega = 1$, $\kappa = 5$).

a_+ and a_- while the NES relative displacement amplitude modulates between b_{++} and b_{--} .

The points b_{++} and b_{--} are found by factoring the SIM, (17), to its roots. In $a_+(a_-)$, the SIM has double root in $b_-(b_+)$. The third root is then $b_{++}(b_{--})$. Equating the root factorization with the SIM equation in a_+ yields:

$$\frac{9}{16} (b^2 - b_-^2)^2 (b^2 - b_{++}^2) = \frac{9}{16} b^6 - 3\Omega^2 b^4 + (\Omega^4 + \xi_{na}^2 \Omega^2) b^2 - \Omega^4 a_+^2. \quad (20)$$

Expanding the left hand side and equating the b^0 terms on both sides gives:

$$b_{++}^2 = \frac{16}{9} \frac{\Omega^4 a_+^2}{b_-^4}. \quad (21)$$

Through the same procedure b_{--} is computed:

$$b_{--}^2 = \frac{16}{9} \frac{\Omega^4 a_-^2}{b_+^4}. \quad (22)$$

3.3 Softening stiffness $f_s(\bar{z}) = \kappa \arctan \bar{z}$

For the softening NES, $f_s(\bar{z}) = \kappa \arctan \bar{z}$, which leads to $G(b) = 2\kappa \frac{\sqrt{b^2+1}-1}{b^2}$. Accordingly, the SIM is:

$$\Omega^4 a^2 = b^2 \left((\Omega \xi_{na})^2 + \left(\Omega^2 - 2\kappa \frac{\sqrt{b^2+1}-1}{b^2} \right)^2 \right). \quad (23)$$

Although $G(b)$ contains a square root, the SIM and Eq. (15), relating the absorber amplitude with the forcing amplitude, can be transformed into a polynomial equation through the substitution $b^2 + 1 = \hat{b}^2$. Equation (15) becomes:

$$\begin{aligned}
& \hat{b}^3 (\Omega^4 (-\sigma + \Omega^2)^2 + \Omega^6 \xi^2 - 2(\sigma - \Omega^2) \Omega^4 \xi \xi_{na} + (\sigma - \Omega^2)^2 \Omega^2 \xi_{na}^2 \\
& \quad - 2\Omega^2 (-\sigma + \Omega^2) (\Omega^4 + \Omega^2 \xi \xi_{na}) + (\Omega^4 + \Omega^2 \xi \xi_{na})^2) \\
& + \hat{b}^2 (-2\Omega^6 (-\sigma + \Omega^2) - 4\kappa\Omega^2(-\sigma + \Omega^2)^2 + \Omega^4(-\sigma + \Omega^2)^2 - 4\kappa\Omega^4\xi^2 + \Omega^6\xi^2 \\
& \quad + 4\kappa(\sigma - \Omega^2)\Omega^2\xi\xi_{na} - 2(\sigma - \Omega^2)\Omega^4\xi\xi_{na} - 2\Omega^4(-\sigma + \Omega^2)\xi\xi_{na} + (\sigma - \Omega^2)^2\Omega^2\xi_{na}^2 \\
& \quad + 2\Omega^4(\Omega^4 + \Omega^2\xi\xi_{na}) + 4\kappa(-\sigma + \Omega^2)(\Omega^4 + \Omega^2\xi\xi_{na}) + 2\Omega^2\xi\xi_{na}(\Omega^4 + \Omega^2\xi\xi_{na}) \\
& \quad - (\Omega^4 + \Omega^2\xi\xi_{na})^2) \\
& + \hat{b} (\Omega^8 + 4\kappa\Omega^4(-\sigma + \Omega^2) + 4\kappa^2(-\sigma + \Omega^2)^2 - \Omega^4(-\sigma + \Omega^2)^2 + 4\kappa^2\Omega^2\xi^2 - \Omega^6\xi^2 \\
& \quad + 2(\sigma - \Omega^2)\Omega^4\xi\xi_{na} + 2\Omega^6\xi\xi_{na} + 4\kappa\Omega^2(-\sigma + \Omega^2)\xi\xi_{na} - (\sigma - \Omega^2)^2\Omega^2\xi_{na}^2 + \Omega^4\xi^2\xi_{na}^2 \\
& \quad - 2\Omega^4(\Omega^4 + \Omega^2\xi\xi_{na}) - 4\kappa(-\sigma + \Omega^2)(\Omega^4 + \Omega^2\xi\xi_{na}) + 2\Omega^2(-\sigma + \Omega^2)(\Omega^4 + \Omega^2\xi\xi_{na}) \\
& \quad - 2\Omega^2\xi\xi_{na}(\Omega^4 + \Omega^2\xi\xi_{na}) - \Omega^4\bar{P}^2) \\
& - \Omega^4\bar{P}^2 - \Omega^8 - 4\kappa\Omega^4(-\sigma + \Omega^2) + 2\Omega^6(-\sigma + \Omega^2) - 4\kappa^2(-\sigma + \Omega^2)^2 + 4\kappa\Omega^2(-\sigma + \Omega^2)^2 \\
& \quad - \Omega^4(-\sigma + \Omega^2)^2 - 4\kappa^2\Omega^2\xi^2 + 4\kappa\Omega^4\xi^2 - \Omega^6\xi^2 - 4\kappa(\sigma - \Omega^2)\Omega^2\xi\xi_{na} + 2(\sigma - \Omega^2)\Omega^4\xi\xi_{na} \\
& \quad - 2\Omega^6\xi\xi_{na} - 4\kappa\Omega^2(-\sigma + \Omega^2)\xi\xi_{na} + 2\Omega^4(-\sigma + \Omega^2)\xi\xi_{na} - (\sigma - \Omega^2)^2\Omega^2\xi_{na}^2 - \Omega^4\xi^2\xi_{na}^2 = 0.
\end{aligned} \tag{24}$$

Only the solutions where $\hat{b} > 1$ are kept, such that $b > 0$ and $\sqrt{b^2 + 1}$ is real.

The maximum and minimum of the SIM are found by deriving (23) w.r.t. \hat{b} , obtaining

$$\begin{aligned}
& \hat{b}^3 (\Omega^4 + \Omega^2\xi_{na}^2) + \hat{b}^2 (2\kappa\Omega^2 + 2\Omega^4 + 2\Omega^2\xi_{na}^2) + \hat{b} (-4\kappa\Omega^2 + \Omega^4 + \Omega^2\xi_{na}) \\
& + 4\kappa^2 - 2\kappa\Omega^2 = 0.
\end{aligned} \tag{25}$$

Considering that $b_{\pm}^2 + 1 = \hat{b}_{\pm}^2$, a_{\mp}^2 is computed as:

$$\Omega^4 a_{\mp}^2 = b_{\pm}^2 \left((\Omega\xi_{na})^2 + \left(\Omega^2 - 2\kappa \frac{\sqrt{b_{\pm}^2 + 1} - 1}{b_{\pm}^2} \right)^2 \right). \tag{26}$$

The SIM and these points for the softening NES are visualized in black in Figure 2.

To compute b_{++} , Eq. (23) is expanded and equated to factoring by roots:

$$\begin{aligned}
& \hat{b}^3 (\Omega^2\xi_{na}^2 + \Omega^4) + \hat{b}^2 (\Omega^2\xi_{na}^2 + \Omega^4 - 4\kappa\Omega^2) + \hat{b} (4\kappa^2 - (1 - a_+^2)\Omega^4 - \Omega^2\xi_{na}^2) \\
& 4\kappa\Omega^2 - 4\kappa^2(1 - a_+^2)\Omega^4 - 4\kappa^2 - \Omega^2\xi_{na}^2 = (\Omega^2\xi_{na}^2 + \Omega^4) \left(\hat{b} - \hat{b}_- \right)^2 \left(\hat{b} - \hat{b}_{++} \right).
\end{aligned} \tag{27}$$

Expanding the right-hand side and equating the \hat{b}^0 terms:

$$\hat{b}_{++} = \frac{4\kappa\Omega^2 - 4\kappa^2(1 - a_+^2)\Omega^4 - 4\kappa^2 - \Omega^2\xi_{na}^2}{\hat{b}_-^2 (\Omega^2\xi_{na}^2 + \Omega^4)} \tag{28}$$

and similarly, b_{--} is computed as:

$$\hat{b}_{--} = \frac{4\kappa\Omega^2 - 4\kappa^2(1 - a_-^2)\Omega^4 - 4\kappa^2 - \Omega^2\xi_{na}^2}{\hat{b}_+^2(\Omega^2\xi_{na}^2 + \Omega^4)} \quad (29)$$

3.4 Frequency responses

Frequency responses (FRs) are computed by fixing the force magnitude \bar{P} and solving (15) to obtain the NES relative displacement b as a function of the excitation frequency Ω . The corresponding host system amplitude a is found through the SIM equation (14). The polynomial forms for the two NESs (18) and (24) allow for a quick computation of the FRs. FRs for several forcing levels, for the hardening and softening stiffness NESs, are provided in Figures 3 and 4, respectively. The thick full and thick dashed lines represent the stable and unstable solutions of the FR. The thin dashed-dotted lines indicate the host system amplitude if no NES were present. Finally, the dotted lines mark the points of interest on the SIM, related to its maxima and minima, as indicated in the figure.

For both NES types, the FR of the host system amplitude a folds around the a_+ -line, effectively leading to a saturation effect. Despite the increase in force, the host system's amplitude does not go above this line. However, this saturation comes at a cost, as IRCs appear to the left (hardening stiffness NES) or right (softening stiffness NES) of the original resonance frequency. The analysis of the IRCs is presented in Section 4.

The FR of the hardening and softening stiffness cannot be compared directly as the values for a and b differ by almost a factor of 10. This is caused by the different scaling in the nondimensionalization procedure, as explained by Eq. (7). As \bar{P} uses the same scaling, it is more suitable to compare the amplification a/\bar{P} and b/\bar{P} , which is illustrated in Figure 5. For the chosen forcing levels, the amplitude saturation near resonance is similar for both NESs. The hardening NES shows an isola, making the softening NES seem like a better choice. However, different forcing amplitude values might lead to different results; therefore, no general conclusion can be drawn with respect to the two Ness comparative performance at this stage. A more thorough comparison of the absorbers' performance is provided in Section 5.

3.5 Strongly modulated response

The frequency responses were computed through the CxA procedure. Previous studies [57, 10] already illustrated the accuracy of the results for the hardening stiffness NES. However, an important phenomenon is not shown by the analytically obtained FR. Around the resonance frequency, the FR presents a branch of unstable solutions, marked by a couple of Nemark-Sacker bifurcations. In this case, the system exhibits a quasi-periodic state where vibration energy is continuously exchanged between the host system and the NES. In the context of NESs, this motion is usually referred to as strongly modulated response (SMR).

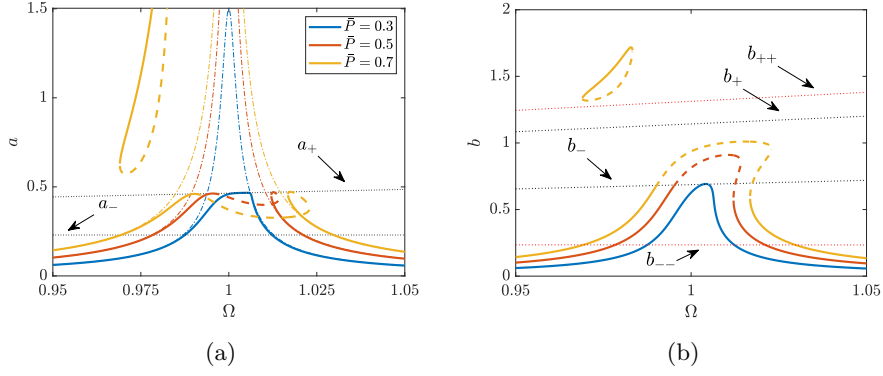


Figure 3: Frequency responses for the hardening NES where $\xi_{\text{na}} = \xi = 0.2$, $\epsilon = 0.02$. The full thick lines represent stable solutions while the dashed lines are unstable solutions.

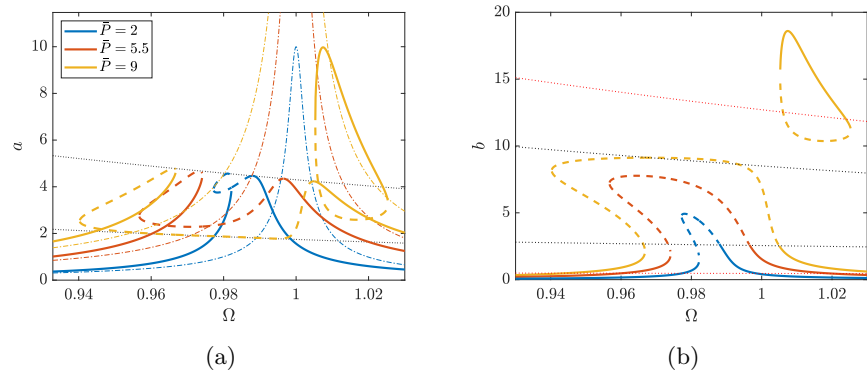


Figure 4: Frequency responses for the softening NES where $\xi_{\text{na}} = \xi = 0.2$, $\epsilon = 0.02$, $\kappa = 5$. The full thick lines represent stable solutions, while the dashed lines are unstable solutions

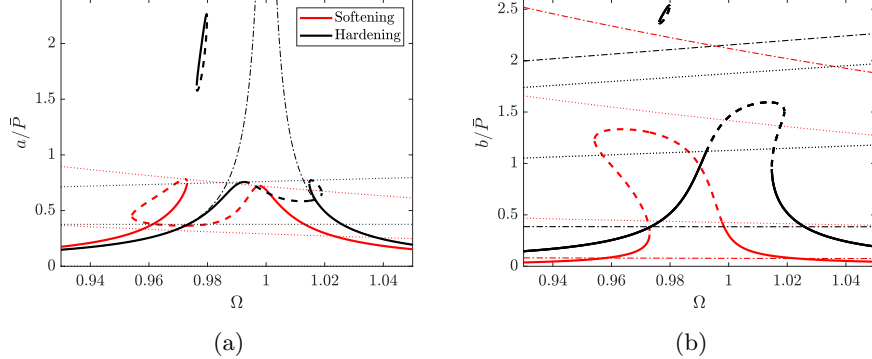


Figure 5: Comparing the amplification a/\bar{P} and b/\bar{P} of the hardening and softening NES where $\xi_{\text{na}} = \xi = 0.2$, $\epsilon = 0.02$ for both NESs and $\kappa = 5$ for the softening NES. For the hardening NES, $\bar{P} = 0.61$ and for softening NES, $\bar{P} = 6$.

The SIM dictates this motion, where the local minima and maxima of the SIM predict the maximal and minimal amplitude of the SMR, and the saturation amplitude of the host system. As this phenomenon was already studied for the hardening NES, in this section, it is verified whether this also holds for the softening NES.

In Figure 6, the time series obtained from a Runge-Kutta (RK) numerical integration of Eq. (8) is shown. The considered parameter values are $\xi = \xi_{\text{na}} = 0.2$, $\epsilon = 0.02$, and $\kappa = 5$. The forcing amplitude is $\bar{P} = 5$ with frequency $\Omega = 0.98$, while trivial initial conditions are used. In Figure 6a, the SMR is exhibited by the modulation of the amplitude of the host system mass displacement \bar{x} . The maximum and minimum of this modulation can be estimated by a_+ and a_- . Regarding the relative absorber displacement \bar{z} , the amplitude modulates between b_{--} and b_{++} . By extracting the envelope from the RK simulations, they can be compared with the SIM in Figure 6b. The SMR has the shape of a continuous cycle: first, it moves up on the SIM left branch, and once it reaches the fold near $[b_-, a_+]$, it jumps to the right branch moving horizontally to the right to $[b_{++}, a_+]$, then it descends the right branch until the fold at $[b_+, a_-]$, from where it jumps back to the left branch to $[b_{--}, a_-]$, where it restarts the cycle. The jumps in the SMR cycle correspond to transient motion between two slowly varying stationary motions on the SIM. Accordingly, while jumping between the stable SIM branches, the numerical solution exhibits a sort of overshoot compared to the analytical SIM. However, while moving on the SIM, the matching between the analytical and numerical solutions is very good, especially for the leftmost part of the SMR cycle.

Simulations are repeated for a range of forcing frequencies in an increasing and decreasing frequency stepped-sine excitation; the obtained oscillation amplitudes are compared to the FR provided by the analytical procedure in Fig. 7. For each simulation, the root-mean-square (RMS) value is computed, and,

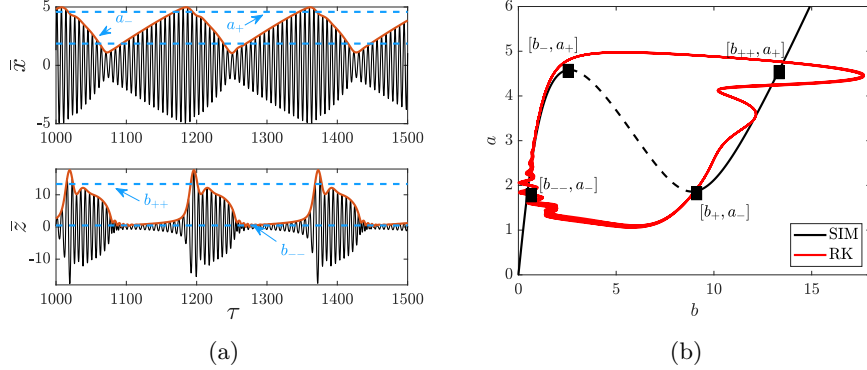


Figure 6: Runge-Kutta simulation of the full EOM for the parameter values $\bar{P} = 5$, $\Omega = 0.98$, $\xi = \xi_{\text{na}} = 0.2$, $\epsilon = 0.02$, and $\kappa = 5$. (a) Time series, (b) SIM and envelope of the time simulation.

if the vibrations exhibit an SMR, the envelope is extracted, and the minimum and maximum are determined from the envelope. The RMS value is multiplied by $\sqrt{2}$, as this should equal the vibration amplitude if the vibrations are a pure sine. The triangles pointing to the right indicate the increasing frequency stepped-sine, while the triangles pointing to the left indicate the decreasing frequency stepped-sine. For periodic solutions (non-SMR), the matching between numerical and analytical solutions is excellent. In the case of SMR, the maximum and minimum of the simulations follow the maximum and minimum of the SIM in black dotted lines for a . Regarding b , the red dotted lines correspond to b_{++} and b_{--} , which mark the maximal and minimal amplitude of the SMRs. Not surprisingly, the minima of the numerical solutions are lower than the analytically predicted minima (in a), while the numerically predicted maxima are larger than the analytical ones (for a and b). This is due to the overshooting of the system during the jump between the two stable branches of the SIM, as also discussed referring to Fig. 6b. Carefully observing the frequency response for $\bar{P} = 5$, Figures 7a and 7b, the increasing and decreasing frequency have a slightly different response. Notably, SMRs also exist for frequency values where the periodic solution is stable. As the analytical FR is computed by assuming a single frequency during the CxA procedure, differences between numerical and analytical results can also be attributed to the contribution of additional frequencies. By increasing the forcing amplitude to $\bar{P} = 9$, an isola appears in the FR, as depicted in Figures 7c and 7d. Although the IRC is detached by the main branch, it is reached by the system during the sweep-up when the branch of SMR ends. In general, reaching the IRC depends on the type of excitation and initial conditions. The relevance of the IRCs is discussed in the next section.

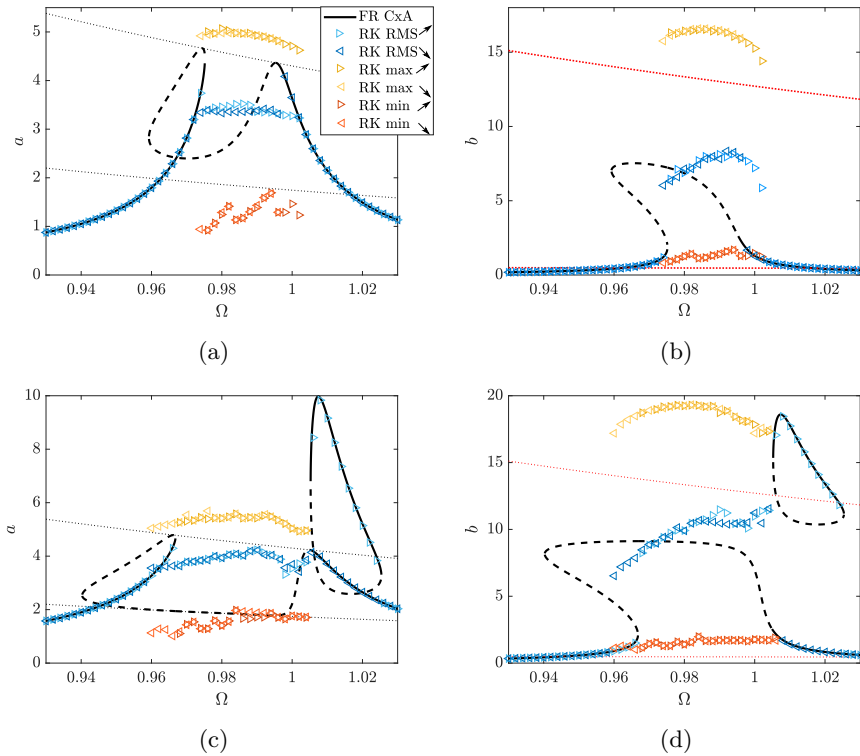


Figure 7: Comparing the RK simulations with the FR obtained from CxA for $\bar{P} = 5$ (a,b) and $\bar{P} = 9$ (c,d). Other parameters are $\xi = \xi_{\text{na}} = 0.2$, $\epsilon = 0.02$ and $\kappa = 5$.

4 Isolated resonance curve analysis

4.1 Singularity theory

For the analysis of the IRCs, we adopt the so-called singularity theory, according to the framework developed in [58] (see also [29], specifically referred to IRC analysis through singularity theory). In simple words, given an equation of the form

$$g(b, \Omega, \mu) = 0, \quad (30)$$

where b is the state variable, Ω is the bifurcation parameter, and μ is a set of parameter values, specific types of topological changes of the curve marked by $g(b, \Omega, \mu) = 0$ can be identified through the evaluation of its implicit derivatives. These topological changes are called singularities and correspond to bifurcations of the original dynamical system. For the scope of this study, two codimension-one nonpersistent singularities are relevant: the isola and the simple bifurcation. The isola singularity, which indicates the appearance of an IRC, marks the boundary between the existence of a closed loop and its inexistence. At the singularity, the IRC is reduced to a single point. Its defining and non-degeneracy conditions are:

$$g = \frac{\partial g}{\partial \Omega} = \frac{\partial g}{\partial b} = 0, \frac{\partial^2 g}{\partial b^2} \neq 0, \det(d^2 g) > 0 \quad (31)$$

where $\det(d^2 g)$ is the determinant of the Hessian matrix.

The simple bifurcation marks the intersection between two branches, distinguishing between the moment when there are, e.g., an upper and a lower branch, from the moment when there is a right and a left branch. At the singularity, the curve appears to be a cross. Concerning the system under investigation, the simple bifurcation marks the merging of an IRC with the main branch (however, it could potentially indicate its detachment). Its defining and non-degeneracy conditions are:

$$g = \frac{\partial g}{\partial \Omega} = \frac{\partial g}{\partial b} = 0, \frac{\partial^2 g}{\partial b^2} \neq 0, \det(d^2 g) < 0. \quad (32)$$

For the systems under study, the algebraic equations describing the system steady-state response are given by Eqs. (18) and (24) for the hardening and saturating cases, respectively. These two equations correspond to the $g(b, \Omega, \mu) = 0$ equation used for the analysis. In order to investigate conditions under which IRCs can appear, a system of algebraic equations, including the defining conditions of isola and simple bifurcations, was created, i.e.,

$$g = 0, \frac{\partial g}{\partial \Omega} = 0, \frac{\partial g}{\partial b} = 0. \quad (33)$$

The solutions of this algebraic equation system are then defined through a classical pseudo-arc length continuation algorithm, leading to curves marking the appearance and merging of the IRC.

4.2 Isolated resonance curve prediction

For the computation, the absorber damping ξ_{na} was kept as a free parameter, obtaining the curves illustrated in Figs. 8a and 8b, which refer to the hardening and softening cases, respectively.

Referring to the hardening case, in Fig. 8a, the upper plot marks the forcing amplitude \bar{P} at which the IRC appears (lower curve) and merges (upper curve). The two cases were distinguished through the sign of the determinant of the Hessian matrix (cf. (31)). The middle plot indicates the frequency at which the IRC appears or merges; we note that the value is always below 1, i.e., at the left of the resonance, as expected. The lower plot illustrates the nondimensional absorber relative oscillation amplitude b at which the IRC appears and merges. The upper curve indicates the appearance of the IRC, while the lower one indicates its merging. An interesting feature of the curves is the fold that they present for $\xi_{na} \approx 0.9$. At the left of this point, no merging or IRC appearance was identified, meaning that, most probably, if $\xi_{na} > 0.9$, the system does not present IRCs. Clearly, variations to the other parameter values modify this limit on ξ_{na} . The values $\epsilon = 0.02$ and $\xi = 0.2$ were used for the computation.

Let us now consider the softening case and the results of the singularity analysis shown in Fig. 8b. The upper plot illustrates forcing amplitude corresponding to the appearance and merging of the IRC, where the lower branch refers to the merging. The middle diagram indicates at which frequency the IRC appears and merges; notably, the values are all above 1, as IRCs are on the right of the resonance peak. The lower plot indicates the nondimensional absorber relative oscillation amplitude at the merging and appearance of the IRC. Also in this case, a fold exists for $\xi_{na} = 0.29$. No IRC should exist on the right side of this fold according to our calculation (we note that the existence of other IRCs not related to the tracked isola singularity cannot be excluded). These results were obtained for $\epsilon = 0.02$, $\xi = 0.2$, and $\kappa = 5$.

Figures 9a and 9b show the two FRs for the hardening NES, one just after the appearance of the IRC ($\bar{P} = 0.604$), and the other one at the merging ($\bar{P} = 1.154$), according to the values obtained in Fig. 8a for $\xi_{na} = 0.2$. The FRs confirm the results obtained through the singularity analysis.

Referring to the softening NES, Figs. 9c and 9d shows the FRs for the appearance of the IRC ($\bar{P} = 8.175$) and its merging ($\bar{P} = 9.573$), according to the value obtained from Fig. 8b. Again, these confirm the accuracy of the singularity analysis. In [44], it was found that for high ξ (damping of the host system), the isola could appear under the saturation line of the host system, a_+ , if the isola stays below b_{++} . In Figures 9e and 9f, it is shown that this is also the case for a saturating NES (here $\xi_{na} = 0.2$, $\xi = 0.5$ and $\kappa = 8$). When the isola just appears, it is below a_+ in the FR of the host system, and below b_{++} in the FR of the absorber. However, increasing the forcing amplitude slightly pushes the isola above b_{++} and above the saturation a_+ . This case will not be investigated further because the high damping of the host system makes it of minimal practical relevance for vibration mitigation, and the force range where

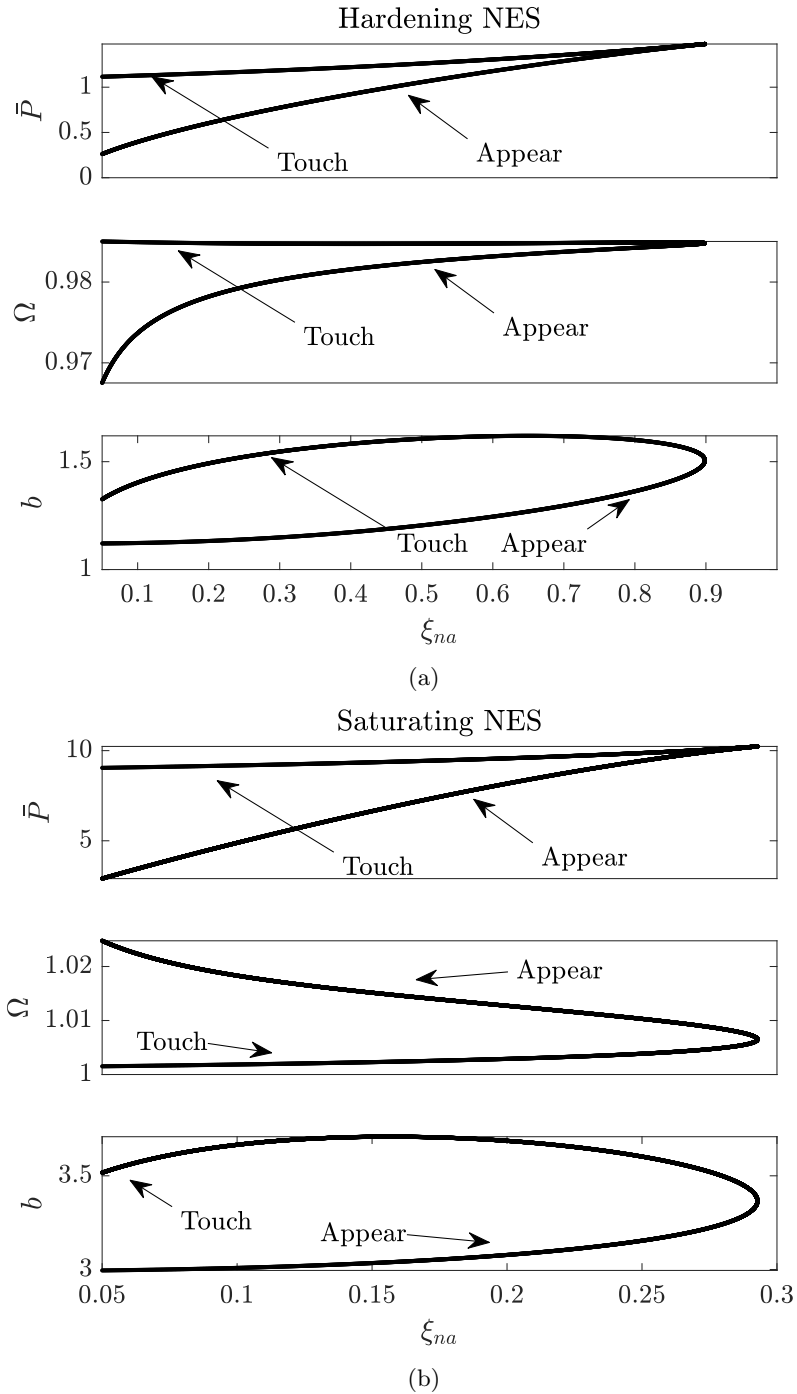


Figure 8: Bifurcation plots for hardening NES ($\xi = \xi_{na} = 0.2$ and $\epsilon = 0.02$) (a) and for the saturating NES ($\xi = \xi_{na} = 0.2$, $\epsilon = 0.02$) and $\kappa = 5$ (b).

the isola is lower than a_+ is rather limited.

5 Comparative performance analysis

5.1 Performance over a force range

The performance of the hardening and softening NES are investigated and compared. Figures 10a and 10b show the maximal amplitude for the softening NES for $\xi = 0.2$, $\epsilon = 0.02$ and $\kappa = 5$, and for the hardening NES for $\xi = 0.2$, $\epsilon = 0.02$. This maximal amplitude is obtained from the maximal value of the FR obtained from the CxA procedure. The bifurcations when the isola appears and merges are also shown on the surface (black lines), as well as the line where the saturation of the amplitude starts (red lines). The condition for the start of saturation of the amplitude a is when b reaches b_- , where accordingly $a = a_+$. This point is found from the following condition:

$$g = \frac{\partial g}{\partial b} = \frac{\partial h}{\partial b} = 0, \frac{\partial^2 h}{\partial b^2} > 0 \quad (34)$$

where g represent either Eq. (18) or Eq. (24), and h indicate the SIM equation, (17) or (23). The surfaces of the NES performance in Figs. 10a and 10b can be divided into 3 parts: 1) For forces lower than the saturation line, the host system oscillation amplitude a increases almost linearly with the force, 2) between the saturation line and isola appearing line the amplitude saturates, and 3) after the isola appearing line, the amplitude increases again in function of the force. Comparing the hardening and saturating NES reveals three main differences: 1) the forcing amplitude leading to saturation almost does not depend on ξ_{na} for the softening NES, while it strongly depends on ξ_{na} for the hardening NES, 2) the plateau of saturation is bigger for the softening NES, and 3) the amplitude jump at the appearance of the isola is larger for the hardening NES than for the softening NES. Sections of these surfaces for $\xi_{na} = [0.2, 0.4, 0.6, 0.8]$ are depicted in Figure 10c for the softening NES and Figure 10d for the hardening NES. These clearly show the increase of amplitude before the saturation, a plateau of saturation, and then a jump, followed by a steady increase of amplitude, once the isola appears. The merging of the isola does not affect the maximal amplitude.

The dashed lines in Figures 10c and 10d mark the a_- value. When the amplitude saturates, an SMR is triggered between the saturated amplitude and a_- . However, for $\xi_{na} = [0.6, 0.8]$, no a_- can be computed because the high NES damping eliminates the folds [7]. Accordingly, for large damping, there will be no SMR and the average amplitude will thus be the maximum amplitude, while under SMR the average or RMS amplitude is between the saturation and a_- . However, increasing ξ_{na} is also beneficial as it increases the force where the isola appears. So, for both NESs, choosing the damping is a compromise between average amplitude and useful force range.

To better compare both NESs, the amplification a/\bar{P} is compared in Figure 11a for the softening NES and in Figure 11b for the hardening NES. Both NESs

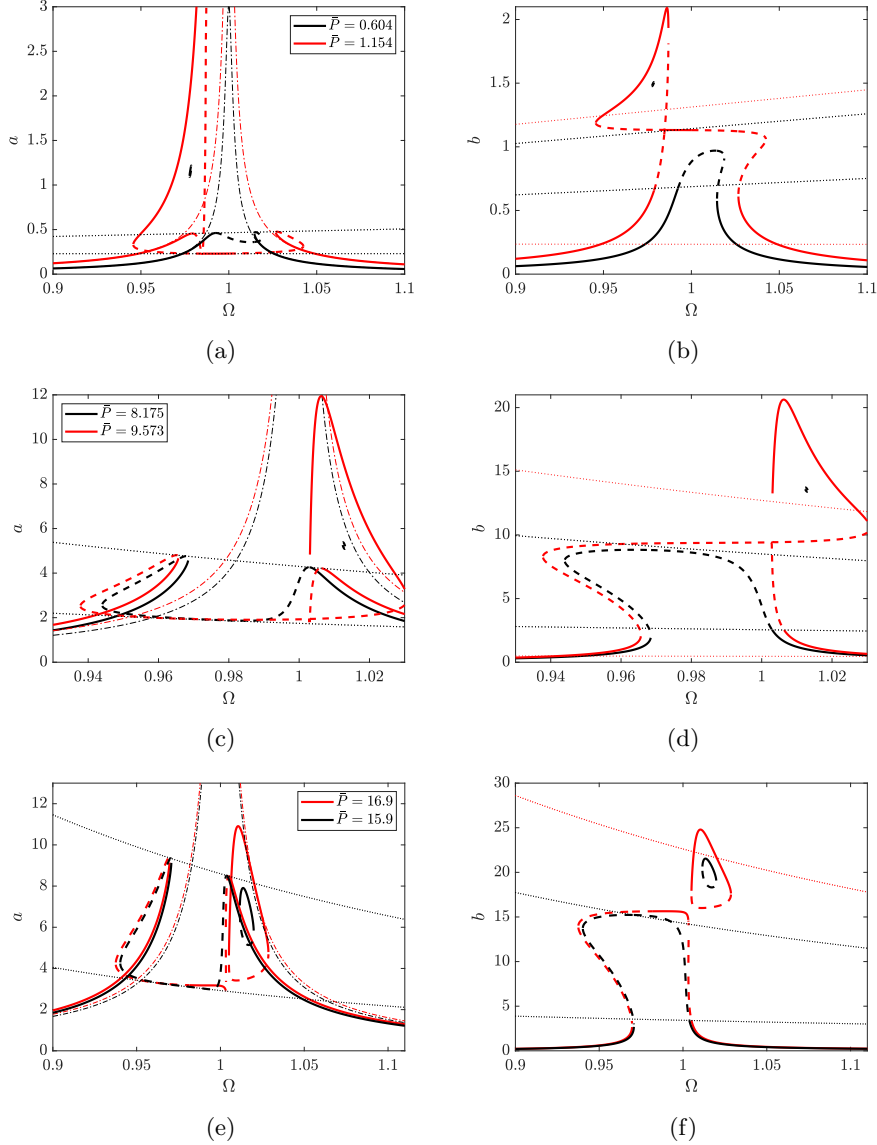


Figure 9: (a,b) Frequency responses for the hardening NES for forcing amplitudes corresponding to appearance merging of the IRC, parameter values: $\xi_{na} = \xi = 0.2$ and $\epsilon = 0.02$. (c,d) Analogous figure for the softening NES, parameter values: $\xi_{na} = \xi = 0.2$, $\epsilon = 0.02$ and $\kappa = 5$. (e,f) Frequency responses for the softening NES in the case for high host system damping, parameter values: $\xi = 0.5$, $\xi_{na} = 0.2$, $\epsilon = 0.02$ and $\kappa = 8$.

are within the same order of magnitude. The softening NES initially has a higher amplification than the hardening one, but for increasing forcing amplitude, it quickly decreases, becoming lower than for the hardening NES. Furthermore, the hardening NES has a large jump as the IRC appears, regardless of its damping. We introduce the force range index (FRI) to further compare the two absorbers:

$$\text{Force Range Index: FRI} = \frac{P_{\text{isola}}}{P_{\text{saturation}}} \quad (35)$$

which is a ratio between the forcing amplitude of IRC appearance and saturating. Since a small saturating force and a large IRC appearance force are desirable, in general, a large FRI is an indicator of good performance. Figure 11c compares this FRI for both NES types. For the hardening NES, FRI first increases and then decreases in function of ξ_{na} , peaking at 2.075; conversely, for the saturating NES, the FRI monotonically increases reaching much higher values than for the hardening NES.

5.2 Optimization

Apart from its mass, the softening NES is defined by two parameters, the damping coefficient ξ_{na} and κ . In Figures 12a-12c, for a given \bar{P} , the maximum amplification a/\bar{P} in the FR is plotted in function of ξ_{na} and κ (excluding unstable solutions). The black lines on the surfaces separate regions where IRC is present from regions where no IRC exists. The lines were obtained through a continuation of the fold in Figure 8b. Note that these lines do not depend on \bar{P} ; these indicate if, for some \bar{P} , an isola exists. The amplification for the hardening NES in function of the damping is also plotted in Figure 12d (excluding its mass, damping is the only parameter defining the dimensionless hardening NES). In the case of softening NES, as the force increases, so do the optimal κ , ξ_{na} and the amplification a/\bar{P} . In each case, the optimal value is just outside the region with IRC. For the hardening NES, the minimum amplification first decreases, then increases in function of \bar{P} . Between the investigated cases, the lowest amplification is obtained for the softening NES, for $\bar{P} = 5$. We remark that the analysis does not take into account SMR, which might be the reason why highly damped NESs seem to provide better performance.

Note that for the hardening NES, the optimal points occur for a damping ξ_{na} where IRC still exists, as the upper Figure 8a indicates the existence of IRCs for $\xi_{na} < 0.9$. While for the optimized \bar{P} , no IRC is present, by increasing the forcing amplitude, an IRC is triggered, which limits the NES performance. Accordingly, an important advantage of the optimized softening NES is the absence of IRC for any forcing amplitude.

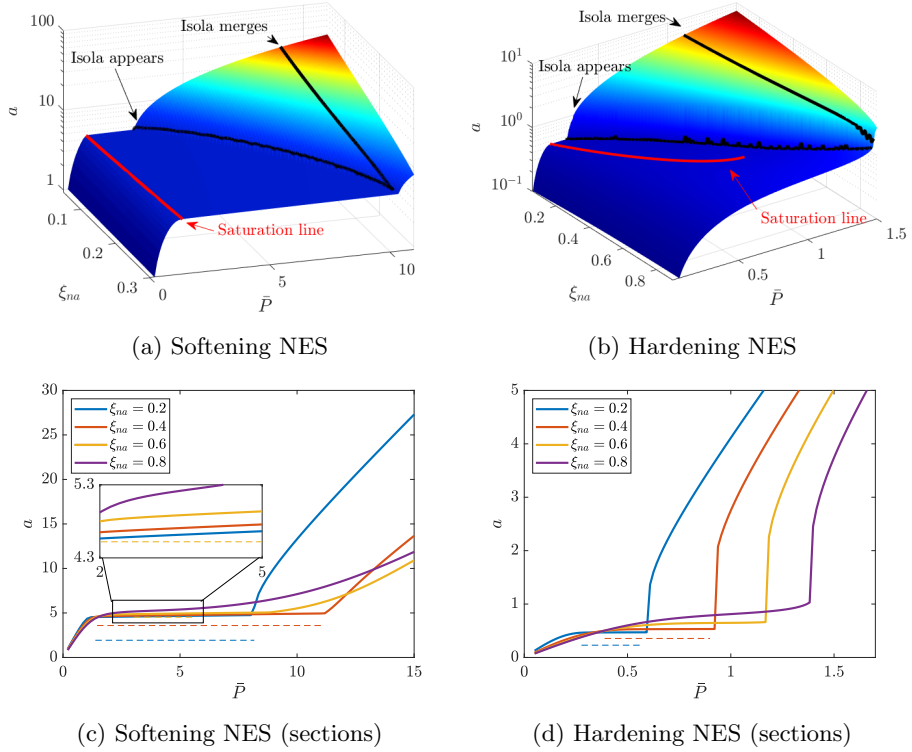


Figure 10: Performance of the NESs interpreted as the maximal amplitude of stable periodic solutions around resonance. Parameter values for the softening NES are $\epsilon = 0.02$, $\xi = 0.2$, and $\kappa = 5$, while for the hardening NES are $\epsilon = 0.02$ and $\xi = 0.2$. Black lines mark the appearance and merging of the isola, while the red lines mark the beginning of the saturation of the host system amplitude. (c) and (d) are sections of the surfaces in (a) and (b), respectively.

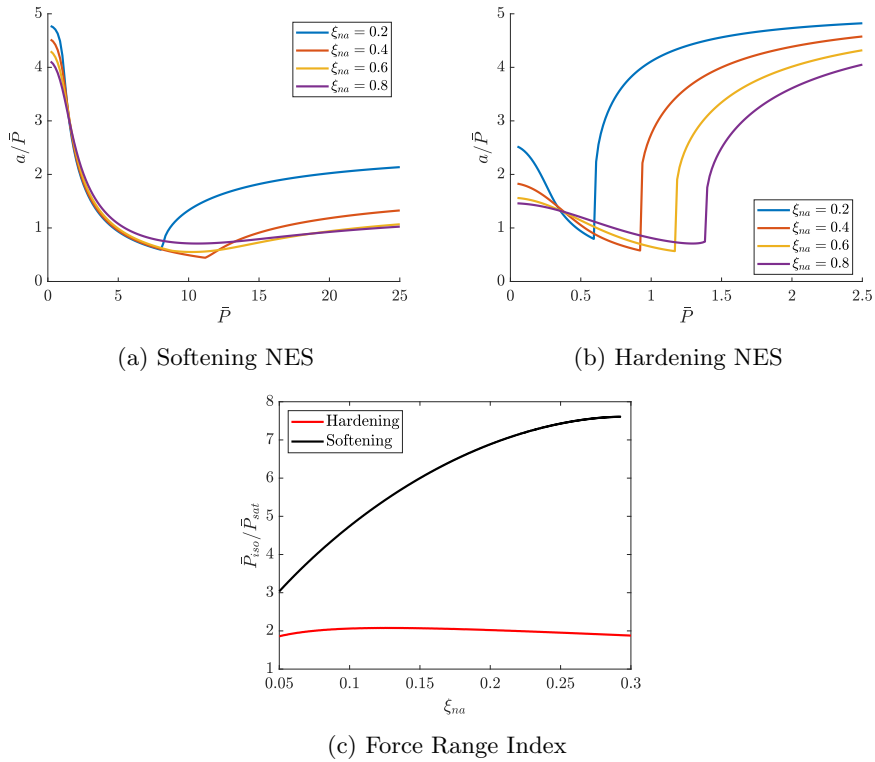


Figure 11: Direct comparison of the amplification a/\bar{P} of the softening (a) and hardening NESs (b), for $\xi = 2$, $\epsilon = 0.02$ for both NESs and $\kappa = 5$ for the saturating NES. (c) Comparison of the Force Range Index for the two absorbers.

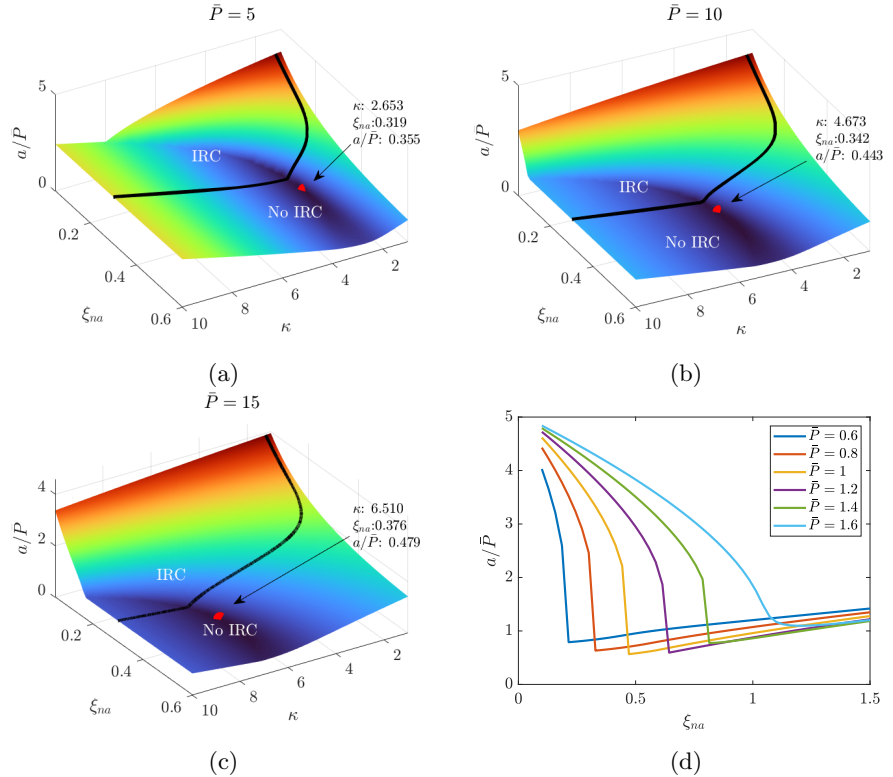


Figure 12: Optimization of \bar{a}/\bar{P} for the softening NES ($\xi = 0.2$, $\epsilon = 0.02$) for $\bar{P} = 5$ (a), $\bar{P} = 10$ (b) and $\bar{P} = 15$ (c); and for the hardening NES ($\xi = 0.2$, $\epsilon = 0.02$)

6 Conclusions

This study investigated the performance of a softening NES and compared it to a conventional hardening NES for harmonically loaded systems. Using the complexification-averaging method, we derived polynomial equations enabling us to analytically investigate system dynamics, focusing on periodic solutions, the saturation effect, SMRs, and IRCs.

Our analysis highlighted several key findings. First, while both softening and hardening NESs exhibit the beneficial saturation effect and SMR, the softening NES demonstrated distinct advantages. The IRC for the softening NES is located to the right of the resonance peak, in contrast to the left-side location for the hardening NES. This rightward placement could benefit systems where the excitation frequency ramps up. Furthermore, the softening NES showed a smaller amplitude jump at the onset of the IRC compared to the hardening NES.

We introduced the Force Range Index (FRI) as a comparative measure of the saturation and isola-appearing force ranges. The softening NES displayed a superior FRI, indicating a broader force range for effective vibration control. Additionally, parameter values were identified where the softening NES operates without IRCs, without compromising its performance. In contrast, eliminating the IRC in a hardening NES requires high damping, which can degrade performance unless nonlinear damping is used [43] — a scenario not addressed in this study.

Overall, the softening NES offers several advantages over the hardening NES, particularly in terms of broader operational force ranges, reduced amplitude jumps, and improved robustness. However, our findings do not preclude the possibility that other forms of nonlinearity might lead to different conclusions. For instance, the interplay of nonlinear stiffness with complex damping mechanisms or alternative restoring force characteristics could yield alternative insights into the comparative performance of softening and hardening NESs. Additionally, while this study focused on theoretical analyses, the practical realization of a softening NES mechanism remains a critical challenge. Developing a robust and scalable implementation of the softening NES, capable of retaining its advantageous properties under real-world conditions, will be an essential step forward. Future research should also extend these investigations to more complex multi-degree-of-freedom systems, where interactions between multiple modes and the NES could introduce new dynamics and further validate the conclusions presented here.

References

- [1] J. Ormondroyd and J. Den Hartog, “The theory of the dynamic vibration absorber,” *Journal of Fluids Engineering*, vol. 49, no. 2, 1928.
- [2] R. Rana and T. T. Soong, “Parametric study and simplified design of tuned mass dampers,” *Engineering structures*, vol. 20, no. 3, pp. 193–204, 1998.

- [3] C.-L. Lee, Y.-T. Chen, L.-L. Chung, and Y.-P. Wang, “Optimal design theories and applications of tuned mass dampers,” *Engineering structures*, vol. 28, no. 1, pp. 43–53, 2006.
- [4] H. Ding and L.-Q. Chen, “Designs, analysis, and applications of nonlinear energy sinks,” *Nonlinear Dynamics*, vol. 100, no. 4, pp. 3061–3107, 2020.
- [5] X.-F. Geng, H. Ding, J.-C. Ji, K.-X. Wei, X.-J. Jing, and L.-Q. Chen, “A state-of-the-art review on the dynamic design of nonlinear energy sinks,” *Engineering Structures*, vol. 313, p. 118228, 2024.
- [6] A. S. Saeed, R. Abdul Nasar, and M. A. AL-Shudeifat, “A review on nonlinear energy sinks: designs, analysis and applications of impact and rotary types,” *Nonlinear Dynamics*, vol. 111, no. 1, pp. 1–37, 2023.
- [7] G. Habib and F. Romeo, “The tuned bistable nonlinear energy sink,” *Nonlinear Dynamics*, vol. 89, no. 1, pp. 179–196, 2017.
- [8] A. F. Vakakis, “Inducing passive nonlinear energy sinks in vibrating systems,” *J. Vib. Acoust.*, vol. 123, no. 3, pp. 324–332, 2001.
- [9] B. Vaurigaud, A. Ture Savadkoohi, and C.-H. Lamarque, “Targeted energy transfer with parallel nonlinear energy sinks. part i: design theory and numerical results,” *Nonlinear dynamics*, vol. 66, pp. 763–780, 2011.
- [10] Z. Wu, S. Seguy, and M. Paredes, “Estimation of energy pumping time in bistable nonlinear energy sink and experimental validation,” *Journal of Vibration and Acoustics*, vol. 144, no. 5, p. 051004, 2022.
- [11] O. Gendelman and T. Bar, “Bifurcations of self-excitation regimes in a van der pol oscillator with a nonlinear energy sink,” *Physica D: Nonlinear Phenomena*, vol. 239, no. 3-4, pp. 220–229, 2010.
- [12] H. Lu, G. Habib, X. Wu, Y. Ren, and L. Yan, “Application of nonlinear energy sink in suppressing wheel shimmy for advanced vehicle chassis design under independent wheel subsystems,” *Nonlinear Dynamics*, pp. 1–17, 2024.
- [13] J. Davidson, T. Kalmár-Nagy, and G. Habib, “Parametric excitation suppression in a floating cylinder via dynamic vibration absorbers: a comparative analysis,” *Nonlinear Dynamics*, vol. 110, no. 2, pp. 1081–1108, 2022.
- [14] B. Bergeot, “Effect of stochastic forcing on the dynamic behavior of a self-sustained oscillator coupled to a non-linear energy sink,” *International Journal of Non-Linear Mechanics*, vol. 150, p. 104351, 2023.
- [15] O. V. Gendelman, “Transition of energy to a nonlinear localized mode in a highly asymmetric system of two oscillators,” *Nonlinear dynamics*, vol. 25, pp. 237–253, 2001.

- [16] A. F. Vakakis, D. M. McFarland, L. Bergman, L. I. Manevitch, and O. Gendelman, “Isolated resonance captures and resonance capture cascades leading to single-or multi-mode passive energy pumping in damped coupled oscillators,” *J. Vib. Acoust.*, vol. 126, no. 2, pp. 235–244, 2004.
- [17] K. Dekemele, R. De Keyser, and M. Loccufier, “Performance measures for targeted energy transfer and resonance capture cascading in nonlinear energy sinks,” *Nonlinear Dynamics*, vol. 93, pp. 259–284, 2018.
- [18] G. Habib and F. Romeo, “Tracking modal interactions in nonlinear energy sink dynamics via high-dimensional invariant manifold,” *Nonlinear Dynamics*, vol. 103, no. 4, pp. 3187–3208, 2021.
- [19] Z. Yan, S. A. Ragab, and M. R. Hajj, “Passive control of transonic flutter with a nonlinear energy sink,” *Nonlinear Dynamics*, vol. 91, pp. 577–590, 2018.
- [20] Y. S. Lee, G. Kerschen, D. M. McFarland, W. J. Hill, C. Nichkawde, T. W. Strganac, L. A. Bergman, and A. F. Vakakis, “Suppressing aeroelastic instability using broadband passive targeted energy transfers, part 2: experiments,” *AIAA journal*, vol. 45, no. 10, pp. 2391–2400, 2007.
- [21] O. Gendelman, Y. Starovetsky, and M. Feldman, “Attractors of harmonically forced linear oscillator with attached nonlinear energy sink i: description of response regimes,” *Nonlinear Dynamics*, vol. 51, pp. 31–46, 2008.
- [22] O. V. Gendelman, E. Gourdon, and C.-H. Lamarque, “Quasiperiodic energy pumping in coupled oscillators under periodic forcing,” *Journal of Sound and Vibration*, vol. 294, no. 4-5, pp. 651–662, 2006.
- [23] H. Abramson, “Response curves for a system with softening restoring force,” *Journal of Applied Mechanics*, vol. 22, no. 3, pp. 434–435, 1955.
- [24] W. Koenigsberg and J. Dunn, “Jump resonant frequency islands in nonlinear feedback control systems,” *IEEE Transactions on Automatic Control*, vol. 20, no. 2, pp. 208–217, 1975.
- [25] R. Bouc, “Influence du cycle d’hystérésis sur la résonance non linéaire d’un circuit série,” in *Colloq. Inter. du CNRS*, vol. 148, 1964, pp. 483–489.
- [26] W. D. Iwan and D. M. Furuike, “The transient and steady-state response of a hereditary system,” *International Journal of Non-Linear Mechanics*, vol. 8, no. 4, pp. 395–406, 1973.
- [27] D. Capecchi and F. Vestroni, “Periodic response of a class of hysteretic oscillators,” *International Journal of Non-Linear Mechanics*, vol. 25, no. 2-3, pp. 309–317, 1990.

- [28] P. Hagedorn, “Parametric resonance in certain nonlinear systems,” in *Periodic Orbits, Stability and Resonances: Proceedings of a Symposium Conducted by the University of São Paulo, the Technical Institute of Aeronautics of São José Dos Campos, and the National Observatory of Rio De Janeiro, at the University of São Paulo, São Paulo, Brasil, 4–12 September, 1969*. Springer, 1970, pp. 482–492.
- [29] G. Habib, G. I. Cirillo, and G. Kerschen, “Isolated resonances and nonlinear damping,” *Nonlinear Dynamics*, vol. 93, pp. 979–994, 2018.
- [30] S. Doole and S. Hogan, “A piece wise linear suspension bridge model: nonlinear dynamics and orbit continuation,” *Dynamics and stability of systems*, vol. 11, no. 1, pp. 19–47, 1996.
- [31] E. Bureau, F. Schilder, M. Elmegård, I. F. Santos, J. J. Thomsen, and J. Starke, “Experimental bifurcation analysis of an impact oscillator—determining stability,” *Journal of Sound and Vibration*, vol. 333, no. 21, pp. 5464–5474, 2014.
- [32] S. Misra, H. Dankowicz, and M. R. Paul, “Degenerate discontinuity-induced bifurcations in tapping-mode atomic-force microscopy,” *Physica D: Nonlinear Phenomena*, vol. 239, no. 1-2, pp. 33–43, 2010.
- [33] G. Rega, “Nonlinear vibrations of suspended cables—part ii: deterministic phenomena,” *Appl. Mech. Rev.*, vol. 57, no. 6, pp. 479–514, 2004.
- [34] S. Lenci and L. Ruzziconi, “Nonlinear phenomena in the single-mode dynamics of a cable-supported beam,” *International Journal of Bifurcation and Chaos*, vol. 19, no. 03, pp. 923–945, 2009.
- [35] M. Volvert and G. Kerschen, “Phase resonance nonlinear modes of mechanical systems,” *Journal of Sound and Vibration*, vol. 511, p. 116355, 2021.
- [36] G. Gatti and M. J. Brennan, “Inner detached frequency response curves: an experimental study,” *Journal of Sound and Vibration*, vol. 396, pp. 246–254, 2017.
- [37] Z. Wu, Y. Zhang, G. Yao, and Y. Yu, “Nonlinear forced vibration and detached resonance curves of axially moving functionally graded carbon nanotube reinforced composite plates,” *Acta Mechanica*, pp. 1–25, 2024.
- [38] A. H. Nayfeh and D. T. Mook, *Nonlinear oscillations*. John Wiley & Sons, 2008.
- [39] T. Detroux, G. Habib, L. Masset, and G. Kerschen, “Performance, robustness and sensitivity analysis of the nonlinear tuned vibration absorber,” *Mechanical Systems and Signal Processing*, vol. 60, pp. 799–809, 2015.

- [40] G. Habib, “Predicting saddle-node bifurcations using transient dynamics: a model-free approach,” *Nonlinear Dynamics*, vol. 111, no. 22, pp. 20 579–20 596, 2023.
- [41] E. Gourdon, N. A. Alexander, C. A. Taylor, C.-H. Lamarque, and S. Pernot, “Nonlinear energy pumping under transient forcing with strongly nonlinear coupling: Theoretical and experimental results,” *Journal of sound and vibration*, vol. 300, no. 3-5, pp. 522–551, 2007.
- [42] G. Cirillo, G. Habib, G. Kerschen, and R. Sepulchre, “Analysis and design of nonlinear resonances via singularity theory,” *Journal of Sound and Vibration*, vol. 392, pp. 295–306, 2017.
- [43] Y. Starosvetsky and O. V. Gendelman, “Vibration absorption in systems with a nonlinear energy sink: nonlinear damping,” *Journal of Sound and Vibration*, vol. 324, no. 3-5, pp. 916–939, 2009.
- [44] E. Gourc, P.-O. Mattei, R. Cote, and M. Capaldo, “Increasing dynamic range of NES by using geometric nonlinear damping,” Mar. 2024, working paper or preprint. [Online]. Available: <https://hal.science/hal-04520466>
- [45] K. Dekemele and G. Habib, “Inverted resonance capture cascade: modal interactions of a nonlinear energy sink with softening stiffness,” *Nonlinear Dynamics*, vol. 111, no. 11, pp. 9839–9861, 2023.
- [46] S. Zhang, J. Zhou, H. Ding, K. Wang, and D. Xu, “Fractional nonlinear energy sinks,” *Applied Mathematics and Mechanics*, vol. 44, no. 5, pp. 711–726, 2023.
- [47] S. Zhang, J. Zhou, H. Ding, K. Wang, and D. Tan, “Theoretical investigation on vibration mitigation in a system with fractional nonlinear energy sinks,” *Nonlinear Dynamics*, pp. 1–23, 2024.
- [48] S. Zhang, J. Zhou, H. Ding, and K. Wang, “Micro-vibration mitigation of a cantilever beam by one-third power nonlinear energy sinks,” *Aerospace Science and Technology*, vol. 153, p. 109409, 2024.
- [49] J. Li, T. U. Rehman, Z. Qaiser, and S. Johnson, “Design optimization and validation of compliant bidirectional constant force mechanisms,” *Mechanism and Machine Theory*, vol. 195, p. 105593, 2024.
- [50] Z. Qaiser, S. Johnson, T. ur Rehman, B. Shun, and Y. Zhou, “Order-of-magnitude increased range of constant force adjustment via section optimization,” *Mechanism and Machine Theory*, vol. 205, p. 105835, 2025.
- [51] H. Nair Prakashah and H. Zhou, “Synthesis of constant torque compliant mechanisms,” *Journal of Mechanisms and Robotics*, vol. 8, no. 6, p. 064503, 2016.

- [52] T. V. Phan, H.-T. Pham *et al.*, “Design and optimization of a large-stroke compliant constant-torque mechanism,” *Journal of Technical Education Science*, vol. 17, no. 1, pp. 93–100, 2022.
- [53] H. Guo, T. Yang, Y. Chen, and L.-Q. Chen, “Singularity analysis on vibration reduction of a nonlinear energy sink system,” *Mechanical Systems and Signal Processing*, vol. 173, p. 109074, 2022.
- [54] L. Manevitch, “The description of localized normal modes in a chain of nonlinear coupled oscillators using complex variables,” *Nonlinear Dynamics*, vol. 25, pp. 95–109, 2001.
- [55] A. F. Vakakis, O. V. Gendelman, L. A. Bergman, D. M. McFarland, G. Kerschen, and Y. S. Lee, *Nonlinear targeted energy transfer in mechanical and structural systems*. Springer Science & Business Media, 2008, vol. 156.
- [56] O. Gendelman, “Targeted energy transfer in systems with external and self-excitation,” *Proceedings of the Institution of Mechanical Engineers, Part C: Journal of Mechanical Engineering Science*, vol. 225, no. 9, pp. 2007–2043, 2011.
- [57] K. Dekemele, “Tailored nonlinear stiffness and geometric damping: Applied to a bistable vibration absorber,” *International Journal of Non-Linear Mechanics*, vol. 157, p. 104548, 2023.
- [58] M. Golubitsky and D. G. Schaeffer, *Singularities and Groups in Bifurcation Theory: Volume I*. New York: Springer Science & Business Media, 1985.
- [59] K. Dekemele, C. Giraud-Audine, and O. Thomas, “A piezoelectric nonlinear energy sink shunt for vibration damping,” *Mechanical Systems and Signal Processing*, vol. 220, p. 111615, 2024.

A Integrals

To compute the integral (16), it is assumed that B is constant over the single period of integration, $Be^{i\Omega\tau} + B^*e^{-i\Omega\tau} = b \cos(\tau + \beta)$. Furthermore, the variable of integration is substituted by $\tau_\beta = \tau + \beta$. When $f_s(\bar{z}) = \bar{z}^3$, this integral is computed as:

$$\begin{aligned} BG(|B|) &= \frac{\Omega}{2\pi} \int_0^{\frac{2\pi}{\Omega}} f_s(Be^{i\tau} + B^*e^{-i\tau}) e^{-i\tau} d\tau \\ &= \frac{be^{i\beta}}{2\pi} \int_0^{\frac{2\pi}{\Omega}} b^2 \cos^3(\tau_\beta) e^{-i\tau_\beta} d\tau_\beta \\ &= \frac{b}{2} e^{i\beta} \left(\frac{3}{4} b^2 \right) = B3|B|^2 \end{aligned} \quad (36)$$

as such, $G(|B|) = 3|B|^2$ and $G(b) = \frac{3}{4}b^2$. For $f_s(\bar{z}) = \kappa \arctan(\bar{z})$ then is:

$$\begin{aligned} BG(|B|) &= \frac{\kappa e^{i\beta}}{2\pi} \int_0^{\frac{2\pi}{\Omega}} \arctan(b \cos(\tau_\beta)) e^{-i\tau_\beta} d\tau_\beta \\ &= e^{i\beta} \left(\frac{\sqrt{b^2 + 1} - 1}{b} \right) = B \left(\frac{\sqrt{4|B|^2 + 1} - 1}{2|B|^2} \right) \end{aligned} \quad (37)$$

B Stability under harmonic load

The stability of the averaged dynamical equations (12) is computed from the linear stability around equilibrium of A and B :

$$2i\sqrt{\Omega^2} \begin{bmatrix} \dot{\Delta}_A \\ \dot{\Delta}_A^* \\ \dot{\Delta}_B \\ \dot{\Delta}_B^* \end{bmatrix} = \underbrace{\begin{bmatrix} a_{11} & a_{12} & a_{13} & a_{14} \\ a_{21} & a_{22} & a_{23} & a_{24} \\ a_{31} & a_{32} & a_{33} & a_{34} \\ a_{41} & a_{42} & a_{43} & a_{44} \end{bmatrix}}_{\Sigma} \begin{bmatrix} \Delta_A \\ \Delta_A^* \\ \Delta_B \\ \Delta_B^* \end{bmatrix} \quad (38)$$

where $\Delta_A = A - A_{\text{eq}}$, $\Delta_B = B - B_{\text{eq}}$ where A_{eq} and B_{eq} are points found in steady-state, (13). The matrix elements are:

$$\begin{aligned}
a_{12} &= a_{21} = a_{32} = a_{41} \\
a_{11} &= -a_{22}^* = -\varepsilon\sigma - i\varepsilon\xi\Omega \\
a_{13} &= -a_{24}^* = i\varepsilon\xi_{na}\Omega + \varepsilon \frac{\partial(B \cdot G(B, B^*))}{\partial B} \Big|_{B=B_{eq}} \\
a_{14} &= -a_{23}^* = \varepsilon \frac{\partial(B \cdot G(B, B^*))}{\partial B^*} \Big|_{B=B_{eq}} \\
a_{31} &= -a_{42}^* = \varepsilon\sigma + i\varepsilon\xi\Omega + \Omega^2 \\
a_{33} &= -a_{44}^* = \Omega^2 - \frac{1+\varepsilon}{\varepsilon}a_{13} \\
a_{34} &= -a_{43}^* = -\frac{1+\varepsilon}{\varepsilon}a_{14}
\end{aligned} \tag{39}$$

The stability is then determined from the eigenvalues of $\frac{\Sigma}{2i\Omega^2}$. The eigenvalues can also be used to determine which type of bifurcation occurs.

C Stability of SIM

To compute the stability of the SIM, a two-time scale method is applied on the dynamical equation of (12) [57, 59]. The two time scales are $\tau_0 = \tau$ and $\tau_1 = \varepsilon\tau$, and the time derivative becomes $'\circ = \partial \circ / \partial \tau_0 + \varepsilon \partial \circ / \partial \tau_1$. After applying the two time-scales the equations are considered per order of ε . For order ε^0 , this is:

$$\begin{aligned}
i2 \frac{\partial A}{\partial \tau_0} \Omega &= 0 \\
i2 \frac{\partial B}{\partial \tau_0} \Omega &= +\Omega^2 B + \Omega^2 A - \xi_{na} i\Omega B + BG(|B|) = 0
\end{aligned} \tag{40}$$

The stability of the solutions on the SIM are computed with the 2nd equation of (40). Linearizing this equation around equilibrium $B_{eq} = \frac{b}{2}e^\beta$ obtained from the solutions of (13) gives the following set of equations:

$$\begin{bmatrix} \dot{\Delta}_B \\ \dot{\Delta}_B^* \end{bmatrix} = \underbrace{\begin{bmatrix} a_{11} & a_{12} \\ a_{21} & a_{22} \end{bmatrix}}_{\Sigma} \begin{bmatrix} \Delta_B \\ \Delta_B^* \end{bmatrix} \tag{41}$$

where $\Delta_B = B - B_{eq}$ where B_{eq} are points on the SIM and

$$\begin{aligned}
a_{11} = a_{22}^* &= -\frac{i\Omega^2}{2} - \frac{\xi_{na}\Omega}{2} + \frac{i}{2} \frac{\partial(B \cdot G(B, B^*))}{\partial B} \Big|_{B=B_{eq}} \\
a_{12} = a_{21}^* &= \frac{i}{2} \frac{\partial(B \cdot G(B, B^*))}{\partial B^*} \Big|_{B=B_{eq}}
\end{aligned} \tag{42}$$

Finally, the stability is determined by computing the eigenvalues of Σ matrix in (41). If any eigenvalue has a positive real part, the solution is unstable.